




Transmissions of an x-ray free electron laser pulse through Al: Influence of nonequilibrium electron kinetics

Cheng Gao ^{1,2,*} Yongjun Li,^{3,†} Fengtao Jin,^{1,2} Jiaolong Zeng ^{1,4} and Jianmin Yuan ^{1,3}

¹Department of Physics, College of Science, National University of Defense Technology, Changsha Hunan 410073, People's Republic of China

²Hunan Key Laboratory of Extreme Matter and Applications, National University of Defense Technology, Changsha Hunan 410073, People's Republic of China

³Graduate School of China Academy of Engineering Physics, Beijing 100193, People's Republic of China

⁴College of Science, Zhejiang University of Technology, Hangzhou Zhejiang 310023, People's Republic of China



(Received 24 April 2024; accepted 12 June 2024; published 2 July 2024)

A theoretical model for investigating the radiative transfer of an x-ray free electron laser (XFEL) pulse is developed based on a one-dimensional radiative transfer equation. The population dynamics of energy levels is obtained by rate equation approximation coupling with the Fokker-Planck equation, in which the electron energy distribution function (EEDF) is self-consistently determined. As an illustrative example, XFEL pulse propagation through a solid-density aluminum (Al) is investigated. The characteristics of the temporal evolution of the x-ray pulse shape, level population, and EEDF are demonstrated. The EEDF usually has two parts in XFEL-Al interactions: the near equilibrium part in the lower energy regions and the nonequilibrium part in the higher energy region. The deep gap between the two parts is quickly filled in the solid-density Al plasma. The pulse shape is distorted and the duration shortens as the x-ray pulse propagates through the Al sample. The x-ray transmission spectra were compared with experimental and other theoretical results, and good agreement was found. There are slight discrepancies between the transmission obtained by solving the Fokker-Planck equation and Maxwellian assumptions because nonequilibrium electrons in the higher energy region account for only a small fraction of the total electrons.

DOI: [10.1103/PhysRevE.110.015201](https://doi.org/10.1103/PhysRevE.110.015201)

I. INTRODUCTION

The investigation of x-ray-matter interaction with x-ray free electron laser (XFEL) applications has attracted considerable attention in the past decade [1–4]. XFEL produces ultrafast ultra-intense x-ray pulses with peak intensities up to 10^{20} W/cm² and durations down to several femtoseconds. Research on XFEL-matter interaction is significant for fundamental investigations and applications such as inner-shell electron dynamics, femtosecond chemistry, and single-particle imaging [5,6]. A number of studies have been conducted on XFEL facilities to investigate ultrafast interactions between x-rays and atoms [7–11], molecules [12–14], clusters [15,16], liquids [17], and solids [18,19].

Irradiated by an ultra-intense x-ray pulse, the inner-shell electron of an atom is primarily ionized (or resonantly excited), leaving core holes which dominantly relax by Auger or radiative decay. The produced photoelectrons and Auger electrons can further interact with ions by impact excitation and ionization. In dense plasmas, electron impact rates can be larger than photoionization rates, which may play a dominant role in level populations. Therefore, an electron distribution function is crucial for determining the rates caused by electron impact processes. Owing to the ultrashort duration of

XFEL pulses, it is difficult for free electrons to arrive at an equilibrium state [20–22]. In the VUV or EUV wavelength region, the nonequilibrium electron kinetics is investigated using different approaches [23–26]. However, only a few studies have been conducted in the x-ray wavelength region [27–31]. For example, Varga *et al.* [28] coupled the rate equation and Fokker-Planck equation to investigate nonequilibrium electronic kinetics in the XFEL-neon plasma interaction, which presented substantial differences in charge state distributions between the equilibrium and nonequilibrium treatment for electrons at relatively high densities. Hau-Riege *et al.* [29] calculated the temporal evolution of electron distribution functions in the XFEL-carbon interaction using molecular dynamics.

Al is a prototype element commonly used in XFEL related studies [32–37], which could serve as a benchmark in understanding the underlying physical mechanism and validating theoretical models. Experimentally, Cho *et al.* [33] studied the reserve saturable absorption of x-ray pulses interacting with Al. Rackstraw *et al.* [35] measured the transmission of XFEL pulses through Al. In their theoretical simulations, free electrons are assumed to reach equilibrium immediately. Theoretically, Royle *et al.* [36] used particle-in-cell methods to investigate x-ray transmission through Al, and the temporal evolution of electron distributions is demonstrated. Recently, Ren *et al.* [37] theoretically studied the influence of nonequilibrium electron distributions on level populations of Al interacting with XFEL pulses. These studies mentioned above

*Contact author: gaocheng@nudt.edu.cn

†Contact author: yjli@gscaep.ac.cn

mainly focused on nonequilibrium electron distributions on level populations. There are few studies of the nonequilibrium effects on x-ray transmission and the underlying physical mechanisms still remain unclear.

In this study, the propagation of an ultra-intense ultrafast x-ray pulse through Al is studied by solving a one-dimensional radiative transfer equation. Attention is paid to nonequilibrium electron kinetics by solving the Fokker-Planck equation, which is self-consistently implemented in a time-dependent rate equation (TDRE). The calculated x-ray transmission is compared with experimental results and other theoretical predictions when available. Further, the effects of nonequilibrium electron kinetics on the level populations, x-ray transmission, and x-ray pulse shape are demonstrated.

II. THEORETICAL METHOD

In this work, we investigate the transmission of x-ray radiation by solving a one-dimensional (assuming along the x axis) radiative transfer equation,

$$\frac{1}{c} \frac{\partial I_\nu}{\partial t} + \cos \theta \frac{\partial I_\nu}{\partial x} = j_\nu \left(1 + \frac{c^2}{2h\nu^3} I_\nu \right) - \mu_\nu I_\nu, \quad (1)$$

where I_ν in $\text{W}/\text{cm}^2/\text{s}^{-1}$ denotes the laser intensity per unit frequency [see Eq. (4)], θ is the incident angle of x rays with respect to the x axis, c is the speed of light, and j_ν and μ_ν denote the emission and absorption coefficients, respectively. In the present study, the elastic scattering process accounts for a very small contribution, which is omitted on the right-hand side of Eq. (1). The absorption coefficient can be expressed as a summation of bound-bound, bound-free (photoionization), and free-free processes. The emission coefficient is expressed similarly. Detailed expressions of the absorption and emission coefficients can be found in Ref. [38].

To determine the absorption and emission coefficients, the level populations are obtained by solving the following rate equation [39–41]:

$$\frac{dn_i}{dt} = \sum_{j \neq i}^{N_L} n_j R_{ji} - n_i \sum_{j \neq i}^{N_L} R_{ij}, \quad (2)$$

where n_i represents the population of level i , R_{ij} and R_{ji} represent the depopulating and populating rates between state i and j , and N_L is the total number of states included in the rate equation. The rates connecting different states include all the main microscopic atomic processes due to photons and electrons, namely, photoexcitation, photoionization, electron impact excitation, electron impact ionization, Auger decay, and their inverse processes. Detailed expressions of the rates can be found elsewhere [38].

The electron impact excitation and ionization rates are obtained by integrating the corresponding cross sections over the electron energy distribution function (EEDF), which is determined by the Fokker-Planck equation,

$$\frac{\partial f(E)}{\partial t} = -\frac{\partial}{\partial E} [a(E)f(E)] + \frac{1}{2} \frac{\partial^2}{\partial E^2} [D(E)f(E)] + S, \quad (3)$$

where $a(E)$ and $D(E)$ denote electron energy exchange and diffusion rates, respectively [42], and S is the source term

representing the electron populations contributed by photoionization, Auger, and relative electron impact processes. The x-ray propagation through a sample is investigated by solving the coupled Eqs. (1)–(3).

The x-ray laser beam is assumed to have a circular spot size on which the intensity has a Gaussian distribution, and the temporal distribution of the intensity is also assumed to be Gaussian. To account for bandwidths of laser pulses (typically 1%) [7], we assume that the laser intensity has a Gaussian distribution with respect to the center x-ray photon frequency. Thus, the laser intensity is frequency dependent. Explicitly, the laser intensity per unit frequency, $I_\nu(r, t)$, at space position r from the laser spot center and time t is expressed as follows:

$$I_\nu(r, t) = I_0 e^{-\ln 2 \left(\frac{r}{\Delta}\right)^2} e^{-\ln 2 \left(\frac{t}{\tau}\right)^2} \sqrt{\frac{\ln 2}{\pi \Gamma^2}} e^{-\ln 2 \left(\frac{\nu - \nu_0}{\Gamma}\right)^2}, \quad (4)$$

where I_0 is the peak intensity in W/cm^2 , ν_0 is the central photon frequency of the x-ray pulse, and Δ , τ , and Γ are the half width at half maximum (HWHM) of the Gaussian distribution profile with respect to space (on the laser spot), time, and photon frequency, respectively.

III. ATOMIC MODEL

Al at room temperature has a filled-shell ionic core ($1s^2 2s^2 2p^6$) with three M -shell electrons in the valence band. We perform the calculation based on an atomic kinetic model. We set the initial states of Al with the help of plasma pictures, i.e., all ions are populated in the ground state ($1s^2 2s^2 2p^6$) of Al^{3+} and the valence band electrons are treated as free electron gas [43]. The ion density is $6.02 \times 10^{22} \text{ cm}^{-3}$ ($2.7 \text{ g}/\text{cm}^3$) and the initial free electron density is $1.8 \times 10^{23} \text{ cm}^{-3}$. The initial state of Al is strongly degenerate, although it can be heated rapidly to a hundred eV by XFEL [32]. For degenerate plasmas, the Pauli exclusion principle plays a role in the electron transition processes, in which the vacancies of free states should be accounted for. In this work, Pauli-blocking factors are introduced to account for electronic degenerate effects in calculating electron-atom impact rates [43], which is expressed as

$$P = 1 - \frac{1}{e^{(E-\mu)kT} + 1}. \quad (5)$$

Here, T is the effective electron temperature, which is defined by $kT = \frac{2}{3n_e} \int E f(E) dE$, with n_e being the total electron density.

The complete set of atomic data, including energy levels, oscillator strengths, photoionization cross sections, electron impact excitation and ionization cross sections, and Auger decay rates is obtained using the FAC code [44]. The corresponding rates of the inverse processes are obtained from the principle of detailed balance. The orbital wave functions in FAC are obtained by solving the Dirac-Fock equation, which is used to construct the configuration wave function. The atomic wave function is expressed as the linear expansions of wave functions of multiconfigurations with the same parity and total angular momentum. Configuration interaction effects are considered in the present calculation. The continuum processes are treated in the distorted wave approximation framework.

TABLE I. Ionization potential (IP) in eV of the ground states of Al^{3+} – Al^{12+} : with (w) and without (wo) IPD.

Ion	Ground config.	IP (wo IPD)	IP (w IPD)
Al^{3+}	$1s^2 2s^2 2p^6$	1601.6	1555.3
Al^{4+}	$1s^2 2s^2 2p^5$	1647.8	1577.9
Al^{5+}	$1s^2 2s^2 2p^4$	1698.4	1608.6
Al^{6+}	$1s^2 2s^2 2p^3$	1753.2	1641.4
Al^{7+}	$1s^2 2s^2 2p^2$	1816.6	1672.0
Al^{8+}	$1s^2 2s^2 2p$	1883.9	1706.0
Al^{9+}	$1s^2 2s^2$	1955.2	1737.2
Al^{10+}	$1s^2 2s$	2016.4	1768.4
Al^{11+}	$1s^2$	2084.9	1792.9
Al^{12+}	$1s$	2304.2	1984.9

In the present work, the K -shell ionization thresholds are crucial and determine whether photoionization can occur. For the solid-density Al, plasma screening effects alter the level structures of atoms embedded in them, resulting into ionization potential depression (IPD). To account for the plasma screening effects, we introduce a self-consistent plasma screening potential into the isolated atomic Hamiltonian (Appendix A), which has successfully predicted IPDs in dense plasmas [45,46]. The energy levels depend on the plasma temperature and density. Plasma states change rapidly in the XFEL-Al interaction, thereby posing a challenge to the calculation for atomic data. Atomic structures are usually more sensitive to plasma density than plasma temperature [47]. Thus the atomic data in this work were obtained under a fixed plasma condition to save the computation cost, i.e., solid density and 180 eV. Under such a plasma condition, the K -shell ionization threshold of the Al^{3+} ionization stage is approximately 1555 eV, which is close to the Al K -edge at room temperature [48]. Such a high temperature can actually be achieved in XFEL heated Al samples [49]. We also checked the IPDs of different charge states and found that they agree with the experimental measurements [46,49]. The K -shell ionization thresholds of different charge states used in the present work are listed in Table 1 (Appendix B). The configurations of different charge states are selected according to the respective IPDs. For Al^{3+} , only the ground configuration $1s^2 2s^2 2p^6$ is considered. For higher charge states, the ground, singly excited configurations, as well as single and double K -shell excited configurations are considered. A complete set of atomic data is obtained for these configurations.

IV. RESULTS AND DISCUSSION

As reported in the experiment [35], the pulse energy is 0.8 mJ with an HWHM duration of 40 fs and a laser spot radial of 1.3 μm . The peak intensity is approximately $1.23 \times 10^{17} \text{ W/cm}^2$. We set $t = 0$ fs as the time when the laser intensity reaches its maximum. The Al sample length is 1 μm . To simulate x-ray transportation, the Al sample is divided into 50 sheets along the x-ray propagation direction (x axis). For each sheet, it is further divided into 20×20 grids. For each grid, the input laser intensity is the output intensity from the corresponding grid in the former sheet. We assume that the interaction of the x-ray pulse with each grid on each sheet is

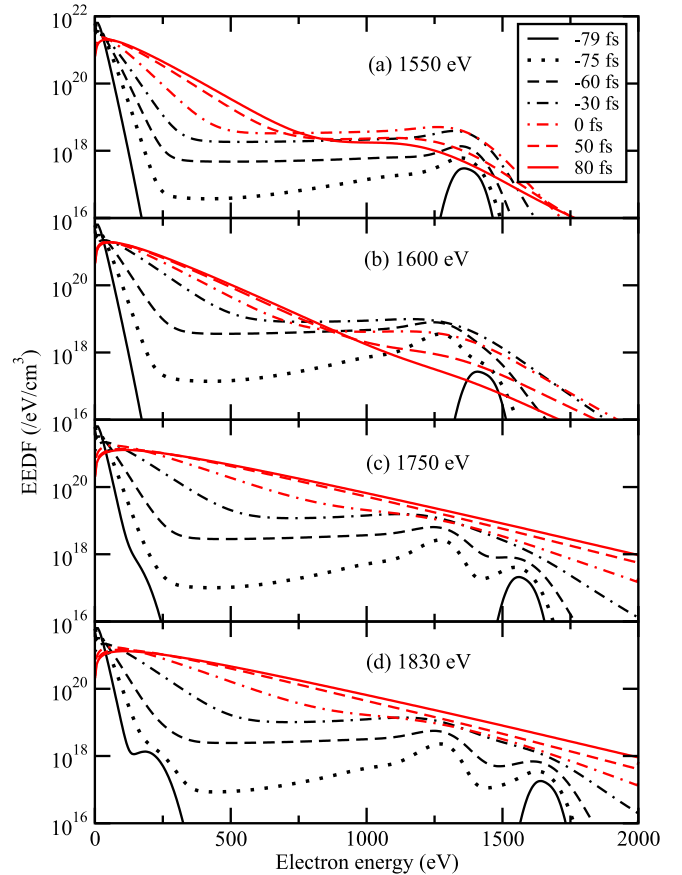


FIG. 1. Time evolution of EEDF on the front of an Al sample ($x = 0 \mu\text{m}$) at the laser spot center with an x-ray photon energy of (a) 1550, (b) 1600, (c) 1750, and (d) 1830 eV. The x-ray pulse energy is 0.8 mJ with a laser spot radial of 1.3 μm . The duration is 40 fs (HWHM) and the laser intensity reaches its maximum ($1.23 \times 10^{17} \text{ W/cm}^2$) at $t = 0$. The laser intensity has spatial and temporal Gaussian distributions.

independent, which means that the level population and EEDF are determined purely by the local incident laser intensity.

Figure 1 shows the time evolution of the EEDF for variable x-ray photon energies. The K -shell threshold of cold Al is approximately 1555 eV [48]. Therefore, x rays with photon energy of 1550 eV [Fig. 1(a)] cannot photoionize K -shell electrons, but mainly L -shell electrons, which results in free electrons ~ 1477 eV. Electrons in the lower energy region are almost still in equilibrium. There is a deep gap between L -shell photoelectrons and initial free electron gas, which are not populated in 300–1250 eV. As time increases, the energy gap is filled very quickly due to electron-electron impact. The EEDF could be divided into two separate parts: the part with electron energy less than 250 eV has an equilibriumlike distribution, while the part with electron energy greater than 250 eV is in obvious nonequilibrium states. The entire EEDF is still in nonequilibrium at the end of the interaction. At an x-ray photon energy of 1600 eV [Fig. 1(b)], the x rays can photoionize the K -shell electrons of Al^{3+} and Al^{4+} , leaving holes in the K shell. The Auger decays of the K holes are dominant decay channels that produce Auger electrons around 1250 eV, slightly below the energy region of L -shell

photoelectrons. The Auger electron populations are much larger than the L -shell photoelectron populations because of the much faster Auger decay rates. Similar to the case for an x-ray photon energy of 1550 eV [Fig. 1(a)], electron collisions quickly flatten the gap between the two parts of EEDF as time increases. However, the EEDF at $h\nu = 1600$ eV approaches equilibrium faster than its counterparts at $h\nu = 1550$ eV. K -shell photoionization rates are much larger than those of L -shell rates. Therefore, more electrons are produced at $h\nu = 1600$ eV. Consequently, electrons collide more frequently and the energy exchange is more efficient, thereby approaching equilibrium faster. The electrons are close to equilibrium at the end of the interaction ($t = 80$ fs).

At a higher x-ray photon energy of 1750 eV [Fig. 1(c)], we can find a shoulder around 200 eV, which are K -shell photoelectrons. The Auger electron populations are evidently larger than the L -shell photoelectron populations, and the two peaks separate from each other compared with the case at $h\nu = 1600$ eV [Fig. 1(b)]. The two peaks rapidly emerge together at approximately $t = -30$ fs. The electrons approach equilibrium even faster than those at lower x-ray photon energies. At the highest photon energy of 1830 eV [Fig. 1(d)], characteristics similar to those in Fig. 1(c) can be seen. The K -shell electrons around 250 eV are clear. From Fig. 1, with a higher x-ray photon energy, the EEDF approaches equilibrium faster. When the x-ray pulse is turned off, free electrons are still far from equilibrium for x-ray photon energy of 1550 eV, while they are nearly in equilibrium for the x-ray photon energy of 1830 eV. Although electrons in higher energy regions can be far from equilibrium, those in lower energy regions are very close to equilibrium. It should be noted that higher energy electrons (1000–2000 eV) account for less than 5% in total free electron number, indicating that the rates of electron impact processes are dominantly contributed by lower energy electrons.

Level populations were obtained by solving rate equations, in which the electron impact excitation and ionization rates were obtained by integrating the EEDF over the corresponding cross sections. As an illustrative example, Fig. 2 shows the temporal evolution of population fractions of different charge states at the laser spot center with an x-ray photon energy of 1750 eV. Figures 2(a) and 2(b) show the population fractions on the front and back sides of the Al sample, respectively. For comparison, the results with Maxwellian distributions (assuming the produced electrons are instantaneously thermalized) are shown by dashed lines. Irradiated by x rays, Al^{3+} is depleted and, accordingly, higher charge states are gradually created. As shown in Fig. 2(a), the depletion of Al^{3+} by solving the Fokker-Planck equation is slower than that by assuming a Maxwellian distribution for free electrons. This can be qualitatively understood by the EEDF characteristics. As discussed in Fig. 1, the fraction of higher energy electrons (> 200 eV) obtained by solving the Fokker-Planck equation is larger than that obtained by assuming the Maxwellian distribution, and thus the fraction of lower energy electrons (< 200 eV) is smaller. Because of the low ionization thresholds of L -shell electrons (~ 73 eV for $2p$ and ~ 118 eV for $2s$ [48]), the EEDF in lower energy regions primarily contributes to the electron collision rates, rather than that in higher energy regions. Thus, the electron impact ionization rates

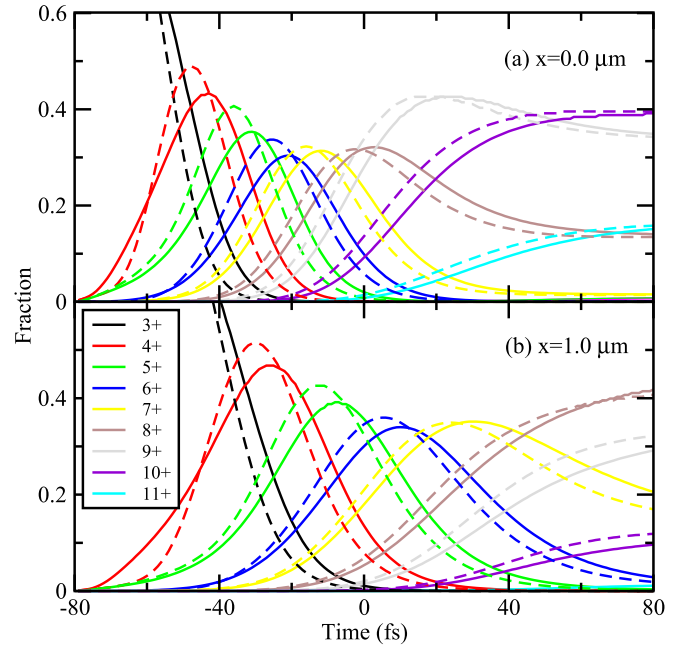


FIG. 2. Time evolution of population fractions at the laser spot center ($r = 0.0 \mu\text{m}$) on the (a) front ($x = 0.0 \mu\text{m}$) and (b) back ($x = 1.0 \mu\text{m}$) of aluminium, respectively. X-ray photon energy is 1750 eV. Solid and dashed lines of the same color represent results by Fokker-Planck and Maxwellian approximations, respectively. The x-ray pulse parameters are the same as Fig. 1.

with nonequilibrium distributions are smaller than those with equilibrium distributions. Consequently, the depletion of Al^{3+} is slower with nonequilibrium distributions. Accordingly, the appearance of higher charge states is later. Notably, the charge state distributions (CSDs) with nonequilibrium distributions (solid lines) are delayed by approximately 10 fs compared with the counterparts with equilibrium distributions (dashed lines).

At the back side of the Al sample, the temporal evolution of CSDs of Al demonstrates characteristics similar to those at the front side. However, Al^{3+} is depleted more slowly. It takes approximately 60 fs and 80 fs for Al^{3+} to deplete at the front and back sides, respectively. For a particular charge state, the width of the population fraction line shape widens as x rays propagate through the sample. The fractions of higher charge states are smaller at the back side. For example, the fraction of Al^{10+} is approximately 40.0% on the front side and 10.0% on the back side, respectively, at the end of the interaction. The fraction of Al^{11+} decreases from approximately 15% to $< 1\%$ as the x rays propagate from the front side to the back side. This is because the x-ray intensity decreases due to absorption as the x-ray pulse propagates through Al.

As the x ray propagates through the Al sample, the x-ray pulse intensity decreases (Fig. 3). Consider the pulse shapes at the laser spot center as an example Fig. 3(a). The intensities of the initial parts of the x rays are much lower than those of the later x rays as the x rays propagate through the Al sample. The x-ray pulse was initially a symmetric Gaussian shape, but it later distorted into an asymmetric shape. Meanwhile, the peak intensity is delayed by approximately 20 fs from the

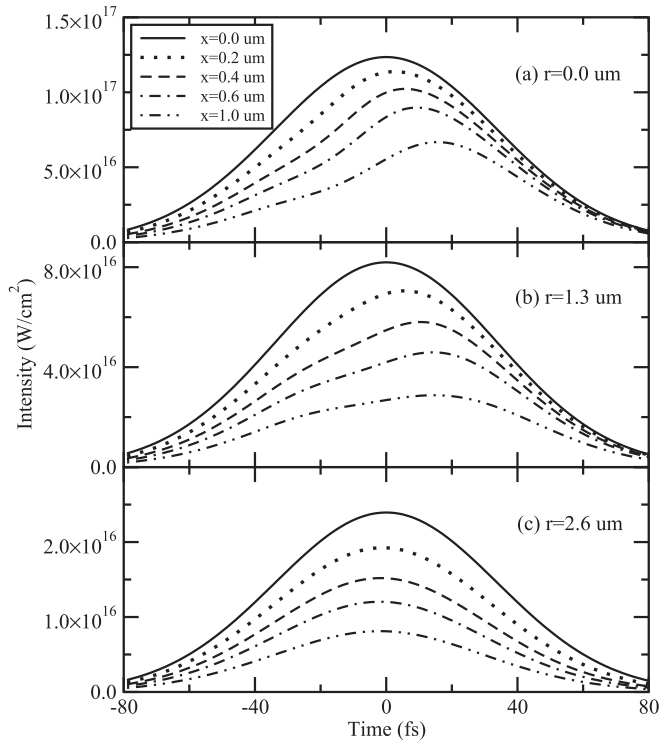


FIG. 3. X-ray pulse shape at the position $r =$ (a) 0.0, (b) 1.3, and (c) 2.6 μm from the laser spot center. In each panel, the pulse shape at different positions (0.0, 0.2, 0.4, 0.6, and 1.0 μm) along the x axis is shown. X-ray photon energy is 1750 eV and other x-ray pulse parameters are the same as Fig. 1.

front side to the back side. The x-ray duration is shortened by approximately 50%, i.e., the initial x-ray duration is 40 fs (HWHM) whereas it is approximately 20 fs when x rays come out of the Al sample. The underlying physical mechanism is easy to understand. K -shell holes are created effectively as x rays irradiate into the Al sample, which decreases the x-ray absorption coefficients compared with the fully occupied K -shell states. Therefore, the initial parts of the x-ray pulse are strongly absorbed, whereas the later parts propagate with much less absorption. Such a phenomenon is the so-called saturable absorption, which is observed in XFEL experiments and is discussed below. The x-ray pulse duration can be shortened using the saturable absorption effect, which has been realized in XFEL-copper interactions [50]. The present calculation demonstrates that duration shortening can also be realized in Al samples.

In the outer laser spot positions, the pulse shape also changes [Figs. 3(b) and 3(c)]. However, the x-ray pulse distortion reduces from the innermost part to the outermost part. The x-ray pulse remains almost symmetric at the outmost part [Fig. 3(c)] and its duration is slightly shortened. The x-ray intensity decreases from the innermost part to the outmost part. The peak intensity at $r = 2.6 \mu\text{m}$ is about 20% of that at the spot center. Thus, fewer K holes are produced, and they are filled up very quickly due to the fast Auger decay rates. The absorption coefficients change slightly during x-ray propagation, which keeps the x-ray pulse shape almost symmetric, as shown in Fig. 3(c).

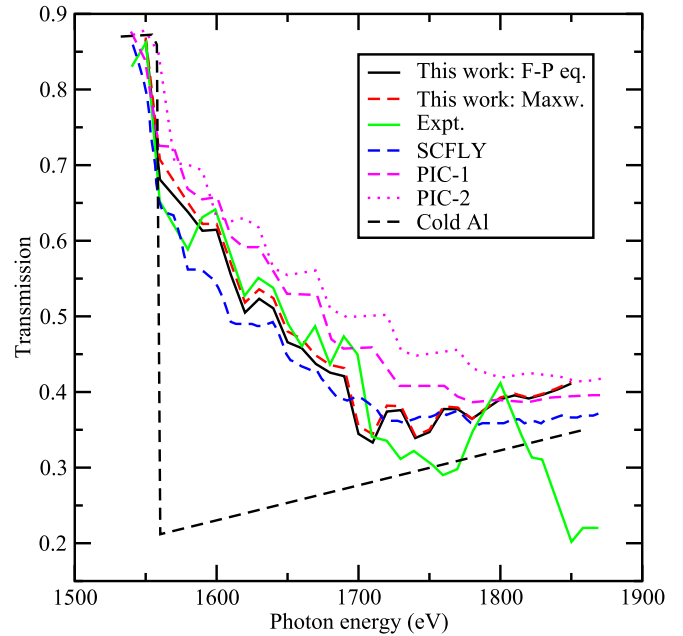


FIG. 4. Transmission of x-ray pulses as a function of photon energy through solid-density Al: comparison with experimental and other theoretical results [35,36]. SCFLY is an atomic kinetic model based on a superconfiguration approximation [35]. PIC-1 and PIC-2 represent PIC simulations [36], which use different IPD formulas (PIC-1 for EK model [52] and PIC-2 for SP model [53], respectively). The black solid and red dashed lines represent the present results with the EEDF obtained by solving the Fokker-Planck equation and assuming a Maxwellian distribution, respectively. Transmission of cold Al is shown as a black dashed line [48]. The x-ray pulse parameters are the same as Fig. 1.

The transmission spectra are helpful for understanding the physical mechanisms during the interaction. The transmission is defined by the ratio of the outgoing to incoming x-ray pulse energy, which is shown as a function of x-ray photon energy (Fig. 4). For comparison, experimental and other theoretical results are shown [35,36]. Compared with the transmission of a cold Al sample, the transmission irradiated by XFEL demonstrates an evident characteristic of saturable absorption. The cold sample transmission decreases sharply when the K -shell threshold is opened, whereas the theoretical transmissions decrease much slower. The K -shell ionization potential of Al^{3+} is 1555 eV, which means that x rays with photon energies less than 1555 eV can only interact with L -shell electrons. The L -shell photoionization cross section is much lower than the K -shell photoionization cross section because the x-ray photon energy is far from the L -shell photoionization thresholds. The K -shell threshold is opened when the x-ray photon energy is greater than 1555 eV and x-ray photons are strongly absorbed, leading to a sharp decrease in transmission. As the x-ray photon energy increases, the K -shell threshold of higher ionization stages opens one by one, and the transmission consequently decreases. The small structures in the transmission spectra correspond to the K -shell opening of different ionization stages. From the inspection of the transmission curve, the K -shell ionization potentials of lowly charged ions agree with the experiment better than the highly

charged ions. The IPDs of Al^{3+} – Al^{6+} are validated to ± 2 eV, while those of Al^{7+} and Al^{8+} are validated to ± 5 eV.

In Ref. [35], a theoretical study was conducted by using SCFLY code [51], which obtains atomic data based on superconfiguration approximations and uses Maxwellian distribution for free electrons. Royle [36] performed a particle-in-cell (PIC) simulation in which electron impact cross sections are obtained using semiclassical methods and nonequilibrium EEDF are considered. Two IPD formulas are used in the PIC methods, i.e., Ecker-Kröll (EK) and Stewart-Pyatt (SP) [52,53]. In general, all three theoretical predictions agree well with the experimental results. SCFLY slightly overestimates x-ray absorptions, whereas PIC methods underestimate them. Our results agree more with the experiment in the photon energy range of 1600–1700 eV. The comparisons indicate the importance of detailed calculation for atomic data. Compared with the experimental results, all theoretical predictions underestimate the x-ray absorption above 1800 eV.

Our transmission results under the assumption that free electrons are a Maxwellian distribution are also shown by the red dashed line. The transmission is very close to the counterpart obtained by solving the Fokker-Planck equation (black solid line). As shown in Fig. 1, the EEDF has two parts: near equilibrium electrons in the lower energy region and far from equilibrium electrons in the higher energy region. However, the number of higher energy electrons is much smaller than that of lower energy electrons. The effect of nonequilibrium higher energy electrons on the rates of electron-atom impact is small. Therefore, the transmission spectra obtained from the two methods are similar. Such a conclusion is consistent with the PIC simulations [36].

V. CONCLUSION

In conclusion, we developed a model to describe ultra-intense and ultrafast x-ray pulses transmission based on a one-dimensional radiative transfer equation. The level populations are obtained by solving a TDRE based on the collisional-radiative model, and free electron distribution functions are self-consistently obtained by the Fokker-Planck equation. The present model is used to simulate an XFEL-Al interaction. Attention is paid to the ultrafast nonequilibrium kinetics of the free electrons in an Al sample interacting with XFEL. Notably, the EEDF can be divided into two parts: the lower energy region is close to equilibrium and the higher energy region is far from equilibrium. EEDF can approach equilibrium states quickly in solid-density plasmas. With higher x-ray photon energies, free electrons approach equilibrium faster at the end of the interaction. Our calculated transmission spectra are compared with experimental and other theoretical results when available. The results agree well. Although high energy electrons are in nonequilibrium, they account for a small fraction of the total electrons, yielding similar x-ray transmission results for the two methods considered in this study.

During the x-ray propagation through an Al sample, the pulse shape is distorted and shortened due to saturable absorption. The duration shortening method based on saturable absorption effects can serve as a different technique to produce ultrashort x-ray pulses [50], which is of great significance for fundamental studies such as inner-shell electron dynamics [54,55].

ACKNOWLEDGMENTS

This work was supported by the National Natural Science Foundation of China under Grant No. 12074430.

APPENDIX A: PLASMA SCREENING POTENTIAL

For an atom embedded in a dense plasma, the orbital wave functions are altered by the plasma screening effects [56]. In the present study, we use our recently developed model to account for the plasma screening effect [57], which reads

$$V_{\text{scr}}(r) = 4\pi \left[\frac{1}{r} \int_0^r r_1 + \int_r^{R_0} \right] r_1 \rho(r_1) dr_1 - \frac{3}{2} \left[\frac{3}{\pi} \rho(r) \right]^{1/3}, \quad (\text{A1})$$

where $\rho(r)$ is the radial distribution of the free electrons in the ion sphere with a radius $R_0 = (3/4\pi n_i)^{1/3}$. Here, n_i denotes the ion density. The last term in the screening potential denotes the finite-temperature exchange-correlation potential [58]. The radial free electron density $\rho(r)$ is expressed as

$$\rho(r) = \frac{1}{\pi^2} \int_{k_0(r)}^{\infty} \frac{k^2 dk}{e^{[\sqrt{k^2 c^2 + c^4} - c^2 + V_{\text{scr}}(r) - \mu]/kT} + 1}, \quad (\text{A2})$$

where k denotes the momentum of free electrons, μ denotes the chemical potential, and c is the light speed in vacuum. The chemical potential μ is determined by the condition of electrical neutrality of the plasma, i.e.,

$$\int_0^{R_0} 4\pi r^2 \rho(r) dr = Z_f, \quad (\text{A3})$$

where Z_f is the mean charge of the plasma.

The screening potential and the electron distributions are coupled with each other, which should be self-consistently solved in an atomic structure calculation. The electron distributions will become uniform in the ion sphere when the temperature is high enough, and thus the present ion-sphere potential will become the commonly used form of

$$V_{\text{scr}} = \frac{Z - N_b}{2R_0} \left[3 - \left(\frac{r}{R_0} \right)^2 \right], \quad (\text{A4})$$

where N_b is the bound electron number [59].

APPENDIX B: K-SHELL IONIZATION THRESHOLDS

The orbital wave functions are obtained by solving the Dirac-Fock equation with plasma screening potential considered. The K -shell ionization thresholds are determined under the plasma temperature of 180 eV and 2.7 g/cm³ (average ionization degree ~ 7), which are listed in Table I.

- [1] C. Bostedt *et al.*, *Rev. Mod. Phys.* **88**, 015007 (2016).
- [2] L. Young *et al.*, *J. Phys. B: At. Mol. Opt. Phys.* **51**, 032003 (2018).
- [3] H. Fukuzawa and K. Ueda, *Adv. Phys. X* **5**, 1785327 (2020).
- [4] C. C. Kao, *Nat. Rev. Phys.* **2**, 340 (2020).
- [5] P. J. Ho *et al.*, *Nat. Commun.* **11**, 167 (2020).
- [6] G. Bortel *et al.*, *Nat. Commun.* **15**, 970 (2024).
- [7] L. Young *et al.*, *Nature (London)* **466**, 56 (2010).
- [8] R. Rudek *et al.*, *Nat. Commun.* **9**, 4200 (2018).
- [9] T. Mazza, M. Ilchen, M. D. Kiselev, E. V. Gryzlova, T. M. Baumann, R. Boll *et al.*, *Phys. Rev. X* **10**, 041056 (2020).
- [10] A. C. LaForge, S.-K. Son, D. Mishra, M. Ilchen, S. Duncanson, E. Eronen *et al.*, *Phys. Rev. Lett.* **127**, 213202 (2021).
- [11] A. Rörig *et al.*, *Nat. Commun.* **14**, 5738 (2023).
- [12] A. Rudenko *et al.*, *Nature (London)* **546**, 129 (2017).
- [13] H. Fukuzawa *et al.*, *Nat. Commun.* **10**, 2186 (2019).
- [14] I. Ismail, A. Ferte, F. Penent, R. Guillemin, D. Peng, T. Marchenko *et al.*, *Phys. Rev. Lett.* **131**, 253201 (2023).
- [15] P. J. Ho and C. Knight, *J. Phys. B: At. Mol. Opt. Phys.* **50**, 104003 (2017).
- [16] Y. Kumagai, Z. Jurek, W. Xu, H. Fukuzawa, K. Motomura, D. Iablonskyi *et al.*, *Phys. Rev. A* **101**, 023412 (2020).
- [17] S. Li *et al.*, *Science* **383**, 1118 (2024).
- [18] K. Tamasaku *et al.*, *Phys. Rev. Lett.* **121**, 083901 (2018).
- [19] M. Harmand, M. Cammarata, M. Chollet, A. G. Krygier, H. T. Lemke, and D. Zhu, *Sci. Rep.* **13**, 18203 (2023).
- [20] R. R. Fäustlin, T. Bornath, T. Doppner, S. Dusterer, E. Forster, C. Fortmann *et al.*, *Phys. Rev. Lett.* **104**, 125002 (2010).
- [21] U. Zastrau *et al.*, *J. Phys. B: At. Mol. Opt. Phys.* **48**, 224004 (2015).
- [22] S. M. Vinko, U. Zastrau, S. Mazevet, J. Andreasson, S. Bajt, T. Burian *et al.*, *Phys. Rev. Lett.* **104**, 225001 (2010).
- [23] B. Ziaja, H. Wabnitz, E. Weckert, and T. Möller, *New J. Phys.* **10**, 043003 (2008).
- [24] N. Medvedev, U. Zastrau, E. Förster, D. O. Gericke, and B. Rethfeld, *Phys. Rev. Lett.* **107**, 165003 (2011).
- [25] D. A. Chapman and D. O. Gericke, *Phys. Rev. Lett.* **107**, 165004 (2011).
- [26] B. Ziaja, J. J. Bekx, M. Masek, N. Medvedev, P. Piekarz, V. Saxena, M. Stransky, and S. Toleikis, *Eur. Phys. J. D* **75**, 224 (2021).
- [27] J. Abdallah Jr and J. Colgan, *J. Phys. B: At. Mol. Opt. Phys.* **45**, 035701 (2012).
- [28] A. G. de la Varga *et al.*, *High Energy Density Phys.* **9**, 542 (2013).
- [29] S. P. Hau-Riege, *Phys. Rev. E* **87**, 053102 (2013).
- [30] C. Gao, Y. J. Li, J. L. Zeng, and J. M. Yuan, *High Energy Density Phys.* **23**, 217 (2017).
- [31] M. S. Cho, H.-K. Chung, M. E. Foord, S. B. Libby, and B. I. Cho, *Phys. Rev. E* **109**, 045207 (2024).
- [32] S. M. Vinko *et al.*, *Nature (London)* **482**, 59 (2012).
- [33] B. I. Cho, K. Engelhorn, S. M. Vinko, H.-K. Chung, O. Ciricosta, D. S. Rackstraw *et al.*, *Phys. Rev. Lett.* **109**, 245003 (2012).
- [34] B. I. Cho, M. S. Cho, M. Kim, H.-K. Chung, B. Barbrel, K. Engelhorn *et al.*, *Phys. Rev. Lett.* **119**, 075002 (2017).
- [35] D. S. Rackstraw, O. Ciricosta, S. M. Vinko, B. Barbrel, T. Burian, J. Chalupsky *et al.*, *Phys. Rev. Lett.* **114**, 015003 (2015).
- [36] R. Royle, Y. Sentoku, R. C. Mancini, I. Paraschiv, and T. Johzaki, *Phys. Rev. E* **95**, 063203 (2017).
- [37] S. Ren, Y. Shi, Q. Y. van den Berg, M. F. Kasim, H.-K. Chung, E. V. Fernandez-Tello, P. Velarde, J. S. Wark, and S. M. Vinko, *Commun. Phys.* **6**, 99 (2023).
- [38] C. Gao, J. L. Zeng, Y. Q. Li, F. T. Jin, and J. M. Yuan, *High Energy Density Phys.* **9**, 583 (2013).
- [39] N. Rohringer and R. Santra, *Phys. Rev. A* **76**, 033416 (2007).
- [40] M. Hantschmann and A. Föhlisch, *J. Electron Spectrosc. Relat. Phenom.* **256**, 147139 (2022).
- [41] K. Toyota, S.-K. Son and R. Santra, *Phys. Rev. A* **95**, 043412 (2017).
- [42] S. Nayakshin and F. Melia, *Astrophys. J. Suppl. Ser.* **114**, 269 (1998).
- [43] B. Deschaut, O. Peyrusse, and F. B. Rosmej, *High Energy Density Phys.* **15**, 22 (2015).
- [44] M. F. Gu, *Can. J. Phys.* **86**, 675 (2008).
- [45] J. Zeng, Y. Li, Y. Hou, C. Gao, and J. Yuan, *Astron. Astrophys.* **644**, A92 (2020).
- [46] J. Zeng, Y. Li, C. Gao, and J. Yuan, *Astron. Astrophys.* **634**, A117 (2020).
- [47] P. F. Liu, C. Gao, Y. Hou, J. Zeng, and J. Yuan, *Commun. Phys.* **1**, 95 (2018).
- [48] B. Henke, E. Gullikson, and J. Davis, *At. Data Nucl. Data Tables* **54**, 181 (1993).
- [49] O. Ciricosta, S. M. Vinko, H.-K. Chung, B. I. Cho, C. R. D. Brown, T. Burian *et al.*, *Phys. Rev. Lett.* **109**, 065002 (2012).
- [50] I. Inoue *et al.*, *Phys. Rev. Lett.* **131**, 163201 (2023).
- [51] H.-K. Chung, M. H. Chen, and R. W. Lee, *High Energy Density Phys.* **3**, 57 (2007).
- [52] G. Ecker and W. Kröll, *Phys. Fluids* **6**, 62 (1963).
- [53] J. C. Stewart and K. D. Pyatt, Jr., *Astrophys. J.* **144**, 1203 (1966).
- [54] E. Lindroth *et al.*, *Nat. Rev. Phys.* **1**, 107 (2019).
- [55] P. K. Maroju *et al.*, *Nature (London)* **578**, 386 (2020).
- [56] M. S. Murillo and J. C. Weisheit, *Phys. Rep.* **302**, 1 (1998).
- [57] Y. Li, J. Wu, Y. Hou, and J. Yuan, *J. Phys. B: At. Mol. Opt. Phys.* **41**, 145002 (2008).
- [58] M. W. C. Dharma-Wardana and R. Taylor, *J. Phys. C: Solid State Phys.* **14**, 629 (1981).
- [59] B. Saha and S. Fritzsche, *J. Phys. B: At. Mol. Opt. Phys.* **40**, 259 (2007).